Interpreting Intensity Speckle as the Coherency Matrix of Classical Light

KyeoReh Lee[1,2,*] and YongKeun Park[1,2,3,†]

[1]*Department of Physics, Korea Advanced Institute of Science and Technology (KAIST), Daejeon 34141, Republic of Korea*
[2]*KAIST Institute for Health Science and Technology, Daejeon 34141, Republic of Korea*
[3]*Tomocube Inc., Daejeon 34109, Republic of Korea*

We show that an intensity speckle can be directly interpreted as the properties of incident light – amplitude, phase, polarization, and coherency over spatial positions. Revisiting the speckle-correlation scattering matrix method [Lee and Park, Nat. Comm. 7, 13359 (2016)], we successfully extract the intact information of incident light from an intensity speckle snapshot as the form of a coherency matrix. The idea is experimentally verified by introducing the peculiar states of light that exhibit uneven amplitude, phase, polarization, and coherency features. We also find substantial practical advantage of the proposed method compared to the conventional coherency matrix measuring techniques such as Stokes polarimetry. We believe this physical interpretation of an intensity speckle could open a new avenue to study and utilize the speckle phenomenon in vast subfields of wave physics.

I. INTRODUCTION

Speckle patterns are the characteristic granular structure that are commonly observed in coherent systems in both unintentional and intentional manners [1,2]. In imaging systems, such granularity has been treated as a noise that significantly reduces image contrast [3–5]; but in speckle metrology, on the other hand, it has been utilized to detect the minute variations in the frequency and wavefront of light [6–12].

Speckle is the consequence of interference that is generally observed when coherent waves pass through complex media such as ground glasses, rough surfaces, and biological tissues, which introduce disordered spatial phase variations [2]. Though it seems arbitrary, the formation of speckle grains is not a random or stochastic process, but a deterministic process. It is predictable if input light and a diffusive optical system are known. In Ref. [13], Popoff et al. demonstrated this by reconstructing the initial optical field from the speckle field, exploiting an optical transmission matrix. They showed that optical diffusers are not fundamentally different from conventional optics, but are the same linear systems having more complex transmission (or reflection) matrices [14]. Accordingly, optical diffusers convey the optical information as in conventional optical systems, but in more scrambled forms – the speckle fields.

One other intriguing feature of speckles is their statistical property. Despite the numerous different situations of speckle generation, the speckle fields mostly show complex Gaussian distributions whose amplitudes follow the Rayleigh distribution [2]. Thus, though it is possible to tailor the odd speckles that follow non-Gaussian statistics using the transmission matrix, immediate return to the Gaussian distribution was observed even by a slight defocus of the detection plane [15]. Such a solid statistical property of speckle enables powerful mathematical tools of Gaussian random variables, which is especially useful in the intensity speckle analyses. A representative example is the Siegert relation that connects the intensity and field correlation of speckles, which has been routinely utilized in dynamic light scattering analyses [16,17] and is also the underlying principle of speckle metrology techniques [18]. However, despite the advantages and usages of intensity speckles, the physical interpretation of such a feasibility has not been clear. What does the intensity speckle represent out of incident light; in other words, how much optical information could be encoded as an intensity speckle and be retrieved from it? In this article, we seek an answer for the question.

In order to the embrace the deterministic and statistical natures of speckle, we revisit the speckle-correlation scattering matrix (SSM) proposed recently [19–21]. The SSM method is a transmission matrix-based holographic technique. Unlike previous works that had presented linear inversion of a transmission matrix from the complex speckle *field* [13,14,22,23], the SSM provides a solid way

———————
*kyeo@kaist.ac.kr
†yk.park@kaist.ac.kr

of achieving the complex incident field from a single *intensity* speckle without reference wave, additional constraints, or multiple measurements [19].

Here, we extend the idea of SSM to the more general properties of classical light. We show that the SSM is a covariance matrix over the space-polarization domain that has been used to define the general state of light including mixed (or partially coherent) states called a coherency matrix [24,25]. Since the SSM is calculated from an intensity speckle without any additional information (notice the transmission matrix is the predetermined constant of the given optical system), we find it is an intensity speckle that determines the entire coherency matrix of light. We also discuss the theoretical and practical constraints of the proposed idea.

The proposed idea is experimentally demonstrated by introducing the general state of light throughout the polarization and mixed states. We also find substantial advantages of the proposed method on the characterization of light compared to the conventional Stokes polarimetry.

II. PRINCIPLE

Let us consider a simple optical setup for intensity speckle measurement (Fig. 1). Assume that the speckle is fully developed and exhibits the Gaussian statistics on the detection plane. Inappropriate selection of a diffuser or a propagation distance between the diffuser and a detector may result in the formation of non-Gaussian speckle [26,27]. Once the setup is fixed, the relationship between incident and speckle fields is firmly determined by the transmission operator, $\hat{t}$ [14,28,29].

Now consider an incident light of pure state $|\psi\rangle$, which is coherent light having a well-defined (static) wavefront and polarization state. It could, therefore, be characterized as a complex-numbered vector, $\psi_e = \langle e|\psi\rangle$, by taking a certain basis $\sum_{e=1}^{N} |e\rangle\langle e| = 1$ of the position-polarization Hilbert space that $|\psi\rangle$ spans. The acquired intensity speckle could be described as $I_x = \beta_x^* \beta_x$, where $\beta_x = \langle x|\hat{t}|\psi\rangle$ is the generated speckle field, while $|x\rangle$ represents the lateral position over the detection plane. Then,
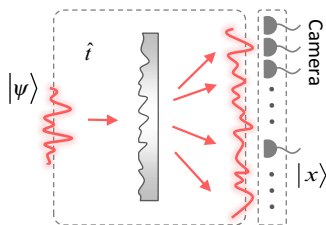

FIG. 1. Intensity speckle measurement. An optical diffuser transforms the incident light into a speckle field. A proper optical diffuser and a propagation length need to be chosen to ensure the complex Gaussian probability distribution of speckle along the $|x\rangle$ space.

the transmission matrix could also be embodied as $t_{xe} = \langle x|\hat{t}|e\rangle$. Note that t_{xe} is also another speckle field over the detection plane for $|\psi\rangle = |e\rangle$. At this point, we introduce the SSM defined by

$$Z_{ij} = \frac{1}{\sigma_i \sigma_j}[\langle t_{xi}^* t_{xj} I_x \rangle_x - \langle t_{xi}^* t_{xj} \rangle_x \langle I_x \rangle_x], \quad (1)$$

where $\langle\rangle_x = \frac{1}{M}\sum_{x=1}^{M}$ and $\sigma_e = \langle t_{xe}^* t_{xe}\rangle_x$ [19]. Utilizing the Gaussian statistics of speckles, the first term of Eq. (1) could be decomposed by the Wick's (or Isserlis') theorem that holds for Gaussian random variables [30]

$$Z_{ij} = \frac{1}{\sigma_i \sigma_j}[\langle t_{xi}^* \beta_x \rangle_x \langle t_{xj} \beta_x^* \rangle_x + \langle t_{xi}^* \beta_x^* \rangle_x \langle t_{xj} \beta_x \rangle_x]. \quad (2)$$

When the number of samplings is large enough to satisfy $M \gg N$, the general orthogonality relations $\sqrt{\frac{1}{\sigma_i \sigma_j}} \langle t_{xi}^* t_{xj} \rangle_x = \delta_{ij}$ and $\langle t_{xi} t_{xj} \rangle_x = 0$ hold in speckle [2]. Then, only the first term in Eq. (2) survives and becomes

$$Z_{ij} = \langle e = i|\psi\rangle\langle\psi|e = j\rangle, \quad (3)$$

which is the shape of the density matrix (in the quantum regime) of the incident light $\hat{\rho} = |\psi\rangle\langle\psi|$ in a given basis $\sum_{e=1}^{N} |e\rangle\langle e| = 1$ [31]. In classical coherence theory, such a covariance matrix has also been utilized to determine the general coherency properties between position and polarization states, called the cross-spectral density (CSD) matrix [24,32] and coherency matrix [24,25], respectively. Although both terminologies may not be adequate for Eq. (3) (because it spans position-polarization space at the same time), we decide to use "coherency matrix" throughout this letter according to several recent works that measured a two-position coherency matrix [33–35].

We also found that Eqs. (1)–(3) are valid in the mixed (or partially coherent) states of light, which are composed of more than one microstates that are incoherent to each other. Such a classical mixed state could be introduced by imposing independent fluctuations on each microstate. For the mixed state, each microstate $|\psi_\alpha\rangle$ generates its own intensity speckle $\beta_{x,\alpha}^* \beta_{x,\alpha}$, which is incoherently summed over the detection plane. Accordingly, the compounded intensity pattern $I_x = \sum_\alpha P_\alpha \beta_{x,\alpha}^* \beta_{x,\alpha}$ is acquired, where P_α denotes the statistical probability of $|\psi_\alpha\rangle$. Substituting the intensity pattern into Eq. (1), one can readily find the corresponding SSM also presents the coherency matrix of the incident mixed states of light, $Z_{ij} = \sum_\alpha P_\alpha \langle e = i|\psi_\alpha\rangle\langle\psi_\alpha|e = j\rangle$. This result implies that a simple optical diffuser in front of the camera is just enough to read the complete optical coherency information of the light over position-polarization space. However, before we proceed, several theoretical and practical constraints should be explored.

First, the speckles β_x or t_{xe} can be non-Gaussian. The optical diffuser should be selected and placed carefully to ensure the Gaussian statistics of speckle on the detection plane (Fig. 1).

Second, the speckles from the different basis vectors may be significantly correlated $\langle t_{xi}^* t_{xj} \rangle_x \neq 0$ for $i \neq j$, which disables the distinguishability between the two different basis vectors and effectively reduces the dimension of measurable Hilbert space. We find such distinguishability is related to the property of the optical diffuser. For example, intensity speckles generated by commercial ground glasses are usually insensitive to the polarization of light, while multiple scattering media are much more sensitive to it [36,37]. In other words, the sensitivity of intensity speckle determines the measurable domain. As several previous works have already proved the sensitivity of intensity speckle to the various properties of light [38–40], we expect the proper selection of diffusers can readily achieve the desired degree of measuring capability. Since multiple scattering usually increases such sensitivity, introducing a scattering medium as a diffuser can be a good choice for the sake of distinguishability. However, it is noteworthy that the multiple scattering usually decreases the transmittance as a tradeoff, which may induce the correlation between different speckles [41–45].

Third, as analyzed in our previous work [19], the oversampling ratio (or M/N), γ plays an important role in noise handling. It was shown that a higher γ is required for stable results as the practical noise level increases. Even in ideal situations without any noise, γ should be larger than four for the safe reconstruction of the pure state due to the inherent noise (the second) term in Eq. (2). For mixed states, we will see that the required γ also increases linearly with the number of microstates in a mixed state or rank$(\hat{Z})$, where $\hat{Z}$ is an operator representation of a coherency matrix. Please notice we utilize an additional error reduction algorithm to rule out such a noise effect (see Appendix A). Note that the generality of our method is still valid since the additional sequence does not require any additional information or free variable as in regularization-based estimation methods [46].

III. EXPERIMENTAL RESULTS

In order to demonstrate the proposed idea, we prepare a compact unit assembled with a camera [Fig. 2(a)]. The unit is composed of only three optical components – an iris, a diffuser, and a polarizer. The iris is added before the diffuser to block ambient light and the polarizer is inserted to fix the detection polarization state. The
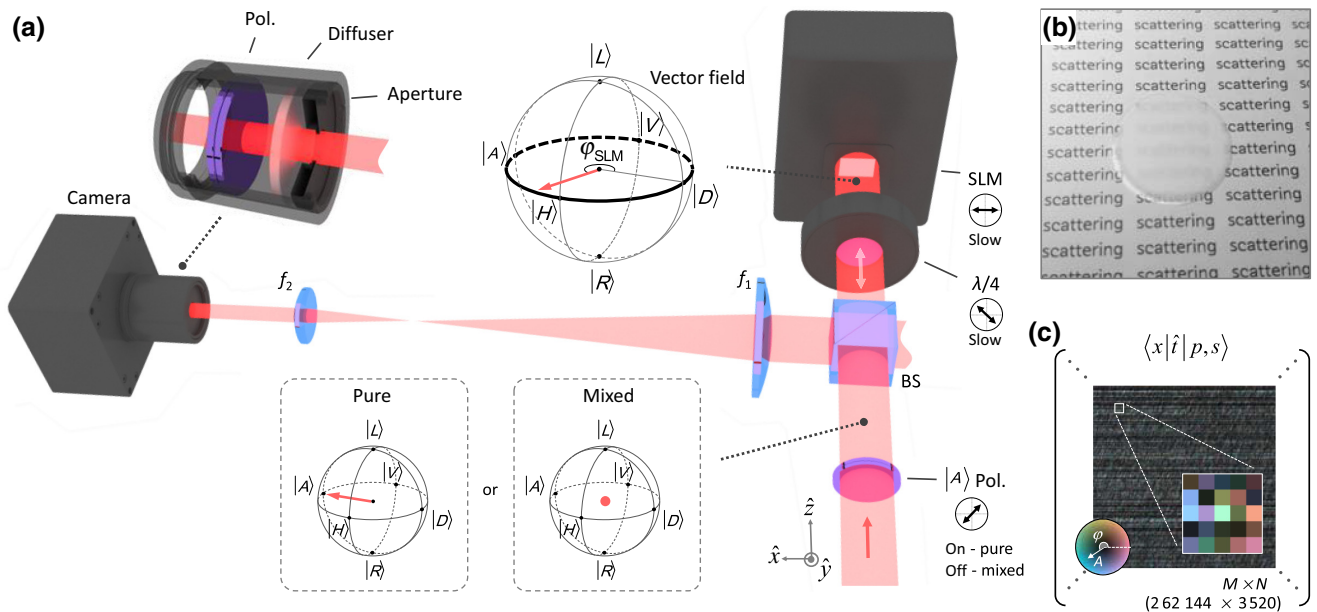

FIG. 2. Experimental setup. (a) The optical setup for preparing and measuring the state of light. The existence of the polarizer in front of the laser determines the prepared polarization state to be either a pure $|A\rangle = \frac{1}{\sqrt{2}}|H\rangle - \frac{1}{\sqrt{2}}|V\rangle$ or mixed $\frac{1}{2}|H\rangle\langle H| + \frac{1}{2}|V\rangle\langle V|$ state. In the case of the pure state, the output polarization state is a function of φ_{SLM}, which varies over the SLM active area. In the case of the mixed state, the SLM phase pattern only modulates the $|s = R\rangle$ state. BS, a 50:50 beam splitter; SLM, a spatial light modulator; $\lambda/4$, a quarter-wave plate; and $f_1 = 300$ mm and $f_2 = 100$ mm. (b) The custom-made diffuser made of rutile nanoparticles. The rutile nanoparticles are deposited on the 25-mm diameter coverslip by a spray painting method. (c) Calibrated transmission matrix t_{xps} of the rutile diffuser. Within the total M-by-N transmission matrix (262 144 × 3520), the central 512 × 512 subpart is displayed. In the color circle, the A and φ denote the amplitude and phase of the complex value in arbitrary and radian units, respectively.

distance between the diffuser and the camera is adjusted to assure that the size of the optical modes (i.e., speckle gain) over the detection plane is larger than the camera pixel size.

A rutile diffuser is introduced in order to maximize the birefringence without sacrificing light transmissivity. We deposit rutile nanoparticles (particle size ≤ 100 nm) on both sides of a coverslip using a spray painting method [Fig. 2(b)].

The manufactured diffuser has a rutile scattering media thickness of 30 μm on both sides of the coverslip (140-μm thickness), mean transmittance of 52% ($\bar{T} = 0.52$), and a transport mean free path of 44.5 μm (see Appendix B). Due to high birefringence ([47], $\Delta n = 0.288$ for 633 nm) and multiple scatterings, we can achieve the complete decorrelation between the speckles from orthogonal polarizations. Accounting for the aperture in front of the diffuser (5.33×4 mm^2, $A = 21.3$ mm^2), the dimensionless conductance of the diffuser can be calculated as $g \approx N_0 \bar{T} = 1.77 \times 10^8$, where $N_0 = 2\pi A / \lambda^2$ is the total number of possible input optical modes. Since $g \gg M$, the mesoscopic correlation is not significantly observed in this work [48].

The transmission matrix of the diffuser is calibrated using a spatial light modulator (SLM), a He-Ne laser, and a Michelson type interferometry [49] (see Appendix C). We select 44×40 plane waves $|p\rangle$ in both horizontal $|H\rangle$ and vertical polarizations $|V\rangle$ as an input basis, $|e\rangle = |p, s\rangle$, ($N = 3520$), and 512×512 central camera pixels $|x\rangle$ as sampling points ($M' = 262\,144$). Thereby, the transmission matrix t_{xps} becomes a $3520 \times 262\,144$ complex-valued matrix [Fig. 2(c)]. According to Eq. (3), the coherency matrices will be presented in the selected basis, and the optical information spans outside the basis will be considered as noise. Due to the practical oversampling of the intensity speckle (i.e., speckle grain > pixel size), the actual number of sampled optical modes M could be smaller than the number of pixels, $M' \geq M$. We figure out that $M = 49\,600$ and $\gamma = 14$ in our experimental scheme by the power spectrum analysis of the acquired intensity speckles (see Appendix D).

A. Pure states

For the first demonstration, we prepare the pure states using a polarized laser source [Fig. 2(a)]. In order to test
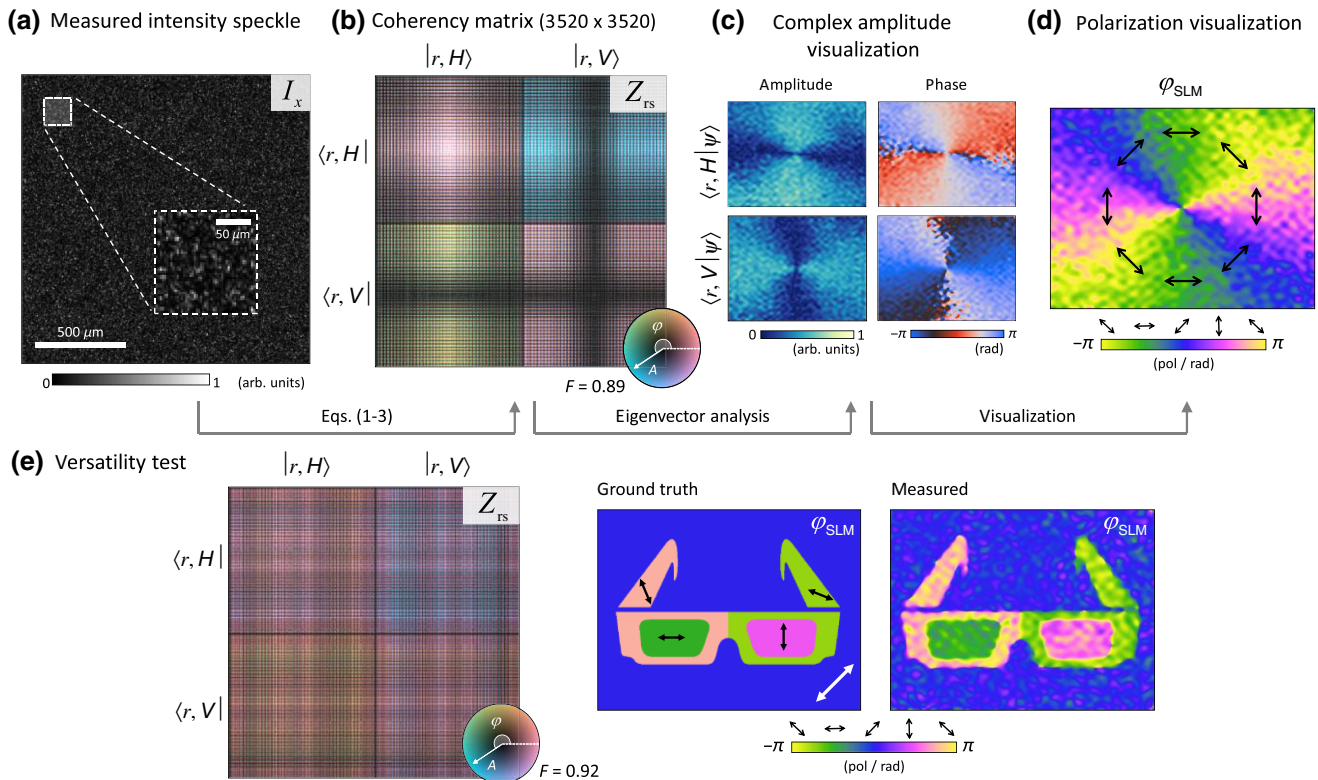

FIG. 3. Experimental demonstrations in pure states. (a) The measured intensity speckle I_x. (b) Retrieved N-by-N (3520×3520) coherency matrix Z_{rs} based on the proposed method. In the color circle, the A and φ denote the amplitude and phase of the complex value in arbitrary and radian units, respectively. (c) The complex coefficients $\langle r, s | \psi \rangle$ extracted from the coherency matrix result. (d) Visualization of the polarization variation over $|r\rangle$, which is related to the displayed SLM phase pattern φ_{SLM}. (e) The measured coherency matrix (left) in the pure state, and the corresponding φ_{SLM} patterns (right) compared with the prepared φ_{SLM} (middle). The fidelity values (F) between the expected and measured coherency matrices are denoted.

the feasibility of the proposed idea, we generate "vector beams" whose polarizations vary over the transversal position $|r\rangle$ [50]. Utilizing a SLM and a quarter-wave plate, we make the polarizations be the function of a given SLM phase φ_{SLM} [Fig. 2(a), Appendix E].

Then, we measure the intensity speckle I_x [Fig. 3(a)], build the SSM using Eq. (1), and calibrate t_{xps}. The detailed procedures for SSM calculation can be found in Ref. [19], and Code 1 [51]. The reconstructed coherency matrices are depicted in Fig. 3(b). For more intuitive visualizations, we use a transversal position $|r, s\rangle$ basis rather than the original plane-wave $|p, s\rangle$ basis by the Fourier transform. By the eigenvecter decomposition of the measured coherency matrix, the complex coefficients $\langle r, s|\psi\rangle$ [Fig. 3(c)] and corresponding φ_{SLM} [Fig. 3(d)] are retrieved according to Eq. (3) and Eq. (E1), respectively. The intended azimuthal polarization vector beam is well reconstructed as shown in Fig. 3(d). We calculate the fidelity $F = |\langle\psi|\psi_0\rangle|^2$ between the expected $|\psi_0\rangle$ and measured $|\psi\rangle$ states to quantify the agreement. We observe consistent high-fidelity values, $F \approx 0.9$, regardless of the displayed SLM patterns [Fig. 3(e)].

B. Mixed states

As a next demonstration, we prepare mixed states. While the overall experimental setup is preserved, the light source is converted to an unpolarized laser [Fig. 2(a)].

We confirm the unpolarized state of light by measuring the Stokes parameters (see Appendix F). Since the SLM with a quarter-wave plate modulates only the $|R\rangle = \frac{1}{\sqrt{2}}|H\rangle - \frac{1}{\sqrt{2}}i|V\rangle$ polarization state, the prepared mixed states become $\hat{Z}_0 = \frac{1}{2}|\psi_L\rangle\langle\psi_L| + \frac{1}{2}|\psi_R\rangle\langle\psi_R|$, where $|\psi_L\rangle$ and $|\psi_R\rangle$ are in two orthonormal polarization states $|L\rangle$ and $|R\rangle$, respectively. Following the same procedures as in pure states, the coherency matrix can be reconstructed by measuring the I_x [Figs. 4(a) and 4(b)]. One simple way to check the validity of the experimental results is to calculate the off-diagonal terms in the circular polarization basis, which are supposed to be zero for the prepared states. As expected, we find the incoherency in Fig. 4(c) by the basis transformation in polarization space. Further, by cropping out the submatrices, we quantify the statistical probabilities P_L and P_R and the complex coefficients, $\langle r|\psi_L\rangle$ and $\langle r|\psi_R\rangle$ of each microstate [Fig. 4(d)]. Note that
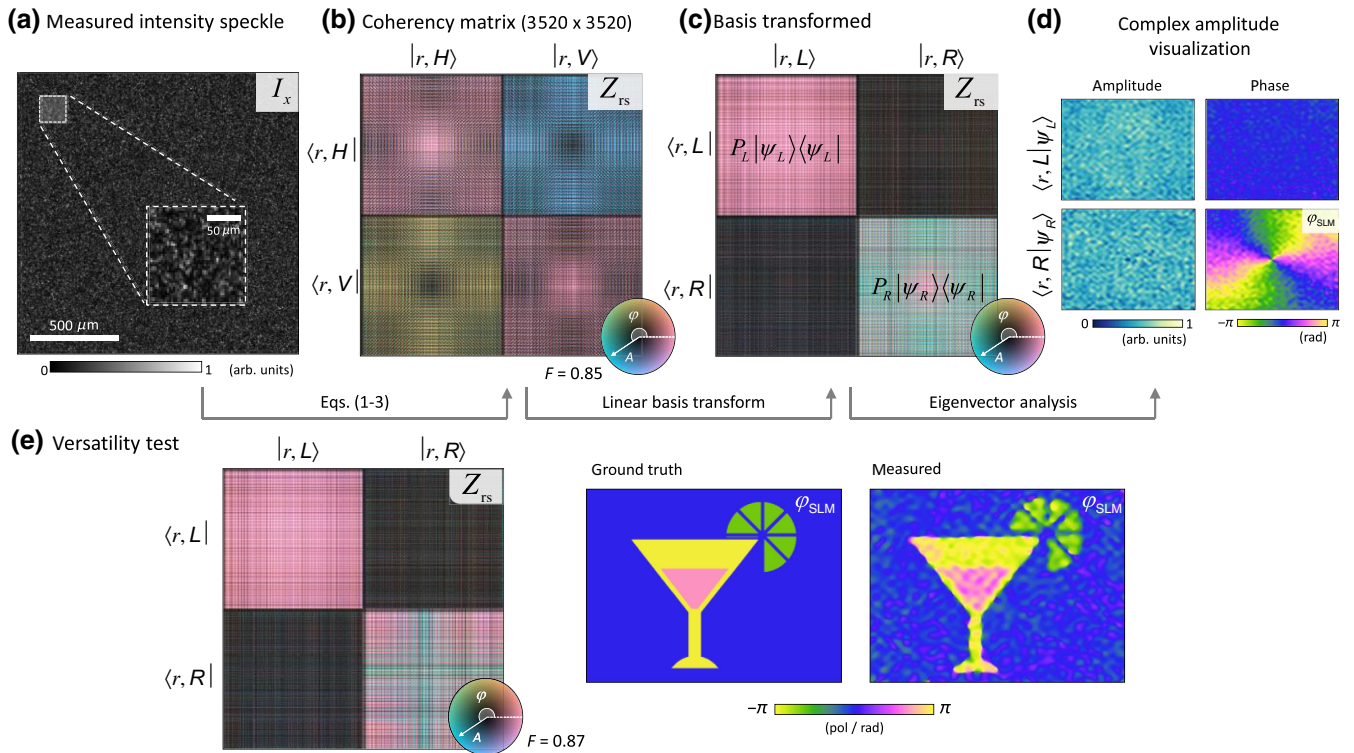

FIG. 4. Experimental demonstrations in mixed states. (a) The measured intensity speckle I_x. (b) Retrieved N-by-N (3520×3520) coherency matrix Z_{rs}, based on the proposed method represented in the $|H\rangle\langle H| + |V\rangle\langle V|$ polarization basis. In the color circle, the A and φ denote the amplitude and phase of the complex value in arbitrary and radian units, respectively. (c) Identical results in $|L\rangle\langle L| + |R\rangle\langle R|$ polarization basis. Here, $P_L = 0.48$ and $P_R = 0.52$ are the measured statistical probabilities of $|\psi_L\rangle$ and $|\psi_R\rangle$, respectively. (d) The two microstates $\langle r|\psi_L\rangle$ and $\langle r|\psi_R\rangle$ cropped out from the coherency matrix are in $|L\rangle$ and $|R\rangle$ polarizations, respectively. Note that only the phase part of the $\langle r|\psi_R\rangle$ is modulated by the SLM. (e) The measured coherency matrix (left) in mixed states, and the corresponding φ_{SLM} pattern (right) compared with the prepared φ_{SLM} (middle). The F between the expected and measured coherency matrices are denoted.

only the phase of the $\langle r|\psi_R\rangle$ is modulated by the SLM. We find that the measured statistical probabilities consistently show $P_L = 0.48$ and $P_R = 0.52$ within a 0.03 standard deviation, which are slightly different from the expectation. Since the optics-derived birefringence or optical activity of the system are calibrated before the measurements using the resting state of SLM (i.e., zero image), we infer such differences are due to the slight reflectivity changes in SLM as the function of an applied voltage. Again, we calculate the fidelity $F = \left[\mathrm{tr}\left(\sqrt{\sqrt{\hat{Z}_0}\hat{Z}\sqrt{\hat{Z}_0}}\right)\right]^2$ between the pre-pared and measured mixed states, $\hat{Z}_0$ and $\hat{Z}$, respectively, to quantify the agreements as proposed in Ref. [52]. We also observe consistent fidelity values, $F \approx 0.85$, regardless of the displayed SLM patterns [Fig. 4(e)]. The lower fidelity values are constantly observed in the mixed state.

In order to elucidate the lower fidelity values in the mixed state, numerical simulations are performed with mixed states having different rank($\hat{Z}$) in various γ. The transmission matrix and complex state of light are arbitrarily generated, but their statistical probability is set uniformly to avoid an effective reduction of rank($\hat{Z}$) from the inhomogeneous probability assignment. From the generated intensity speckle, the reconstruction of the

coherency matrix is done by the proposed way, and the fidelity of the reconstructed field is calculated to quantify the performance, as we show in Code 1 [51]. We find the required oversampling ratio γ_c (for $F > 0.95$) linearly increases with rank($\hat{Z}$) as $\gamma_c \approx 4 \cdot \mathrm{rank}(\hat{Z})$ even in noise-free circumstances (Fig. 5), which supports our experimental results. As expected, practical noises could further increase the γ_c, while the positive correlation property to rank($\hat{Z}$) remains the same. Notice that for optical systems having $g \approx M$, the mean transmittance and the condition number of the transmission matrix may also affect the achievable fidelity (see Appendix G).

Until today, Stokes polarimetry has been a conventional way to measure the general state and degree of polarization [53]. It consists of four-phase shifting measurements in a given spatial mode, and the measured Stokes vectors are directly related to the four elements of a coherency matrix, $\langle r_0, H|\hat{Z}|r_0, H\rangle$, $\langle r_0, H|\hat{Z}|r_0, V\rangle$, $\langle r_0, V|\hat{Z}|r_0, H\rangle$, and $\langle r_0, V|\hat{Z}|r_0, V\rangle$, which is also equal to a common 2×2 coherency matrix [25]. We find the same strategy can be extended to measure a general $N \times N$ coherency matrix but it now requires at least four measurements per each $\langle r_1, s_1|$ and $|r_2, s_2\rangle$ pair. This is not impossible, but is going to be very tedious, especially due to the scanning spatial mode pairs. For example, our results ($N = 3520$) could be retrieved by the conventional Stokes polarimetry with $2N(N\text{-}1) = 24\,773\,760$ individual measurements. Therefore, we expect that the proposed method may create a practical advantage in the characterization of the general multimode state of light due to its single-shot nature.

IV. CONCLUSION

In conclusion, we show that the SSM can be interpreted as the coherency matrix of classical light. Since the transmission matrix is a constant that is predetermined by the prepared diffusive optical system, we can deduce that the coherency matrix of light is entirely presented by the measured intensity speckle. The idea is experimentally verified in the general state of light throughout the polarization and mixed states. The required oversampling ratio is numerically explored in a different number of microstates. Compared with the conventional Stokes polarimetry, we find that the proposed idea could have a substantial advantage in the simultaneous multimodal determination of a coherency matrix.

We expect the present method will open alternative approaches for the study of wave physics and its application to various disciplines. Because the formation of speckle is fundamentally governed by the wave equations and is ubiquitous in various subfields of wave physics, we expect this idea could be generally expanded to the speckles made of different waves such as ultrasound [54], microwave [55], and x-ray [56].
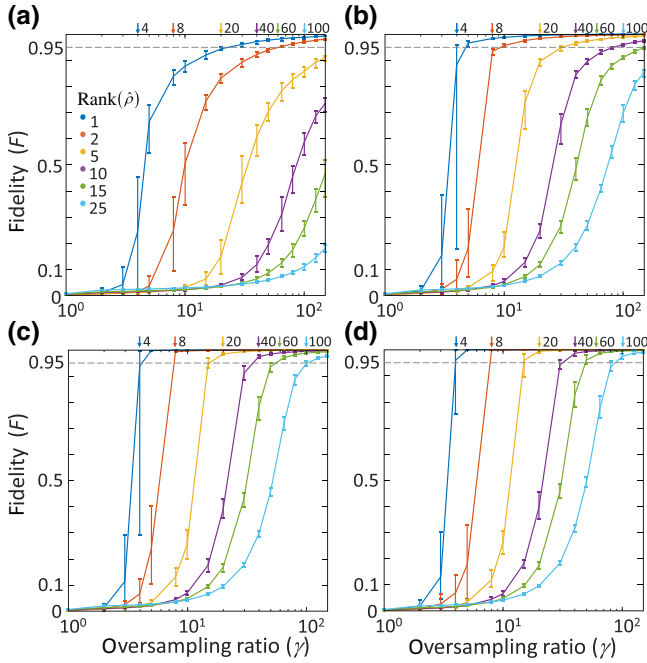

FIG. 5. Numerical fidelity results in shot-noise limited situations. The practical shot-noise is introduced by the finite full well capacity (Π) of the camera. For given Π − (a) $\Pi = 10$, (b) $\Pi = 10^2$, (c) $\Pi = 10^3$, and (d) $\Pi = \infty$ − the shot-noise-limited signal-to-noise becomes $\sqrt{\Pi}$ for the brightest pixels. All fidelity results are calculated after the error reduction algorithm. The error bars represent the 95% confidence intervals of 25 numerical results. Downward arrows above indicate $\gamma = 4 \cdot \mathrm{rank}(\hat{Z})$.

Yet, for the wider utilizations of intensity speckles as a routine light analysis tool, the stability of a diffusive system and the reconstruction speed and robustness of a coherency matrix should be further improved. We expect the issues can be remedied by the introduction of the designed diffusers [21,57,58] and advanced nonlinear equation solvers, respectively.

ACKNOWLEDGMENTS

APPENDIX A: ERROR REDUCTION ITERATIVE ALGORITHM

To suppress fundamental errors and practical noises, we utilize the Gerchberg-Saxton (GS) type iterative algorithm, while the Fourier transform in the original GS algorithm is replaced by the transmission matrix t_{xe}. For each iteration step, the algorithm consists of three substeps. First, the basis of the coherency matrix is transformed from $|e\rangle$ to $|x\rangle$ (camera pixel basis) by the transmission matrix, $Z_x = t_{xe} Z_e t_{ex}^+$, where t_{ex}^+ is the pseudoinverse matrix of t_{xe} that satisfies $t_{ex}^+ t_{xe} = 1_e$. Second, Z_x is updated to $Z_x^\bullet$ by utilizing the measured intensity speckle I_x as a constraint. The amplitude part of Z_x is revised, while the phase part is conserved. Third, the coherency matrix is updated by the inverse basis transform, $Z_e^\bullet = t_{ex}^+ Z_x^\bullet t_{xe}$. The iteration starts from Eq. (3) and stops when the coherency matrix converges; the correlation between Z_e and $Z_e^\bullet$ reaches 0.999 998. In conclusion, the iterative algorithm reduces error by converging the closest local minimum of a given intensity image I_x using Eq. (3) as an initial guess. Note that proposed iterative algorithm does not require any additional information or free variables.

APPENDIX B: CUSTOM RUTILE DIFFUSER

The custom rutile paint is made by mixing rutile nanoparticles (637262, Sigma-Aldrich Co. LLC.) with resin (RSN0806, DOW CORNING®, $n \approx 1.5$) and solvent (toluene, 99%) in a proper ratio (0.5 g:1 mL:10 mL). In order to disperse the rutile nanoparticles, we sonicate the paint for 10 min. The rutile paint is deposited on both sides of the 25-mm diameter and 140-μm thick round coverslip by the spray painting method using a commercial airbrush (DH-125, Sparmax). After the spray painting, the diffuser is baked (100°C, 10 min) to cure the resin. The diffuser has a thickness of 30 μm per side, a mean transmittance of 52% ($\bar{T} = 0.52$), and a transport mean free

path of 44.5 μm. The transmissivity and transport mean free path of the diffuser are measured by the integrating sphere (UPK-100-F, Gigahertz-Optik) using the inverse adding-doubling method.

APPENDIX C: TRANSMISSION MATRIX CALIBRATION

Figure 6(a) shows the experimental setup for the transmission matrix calibration. The transmission matrix t is the collection of the speckle field for the specific input states $|\psi\rangle = |p, s\rangle$ measured in the $|x\rangle$ space. Therefore, we produce the $|p, s\rangle$ states using a SLM (X10468-01, Hamamatsu photonics K.K.) and a liquid crystal variable retarder (LCVR; LCC1222-A, Thorlabs Inc.).

The plane waves $|p\rangle$ are prepared by displaying phase ramps on the SLM. We select a 44×40 central area of the reciprocal domain of the SLM. The allocated transversal momentum for the $|p = n\rangle$ state is the nth component of a vectorized 44×40 matrix [Fig. 6(b)]. The polarization state $|s\rangle$ is prepared by the LCVR by adjusting the phase retardance.

Since our SLM only modulates the $|s = H\rangle$ state, we achieve output polarization states $|H\rangle$ and $|V\rangle$ for 0 and π phase retardations, respectively. Therefore, a total of $44 \times 40 \times 2$ $|p, s\rangle$ states ($N = 3520$) are prepared.

In order to measure the complex numbers t_{xps}, we construct a Michelson type interferometer using a He-Ne laser (HNL050R, Thorlabs Inc.). The reference arm also supplies a static reference speckle field over the detection plane, $R_x = \langle x|\hat{t}|\text{ref}\rangle$.

Using the phase shifting concept, we achieve the interference term $R_x^* t_{xps}$. For each $|p, s\rangle$ input state, we take three images $I_{x,0}$, $I_{x,1}$, and $I_{x,2}$, while the SLM displays $|p, s\rangle$, $|p, s\rangle e^{i(2\pi/3)}$, and $|p, s\rangle e^{-i(2\pi/3)}$, respectively. Then, the interference term can be calculated as follows: $R_x^* t_{xps} = \frac{1}{3}[I_{x,0} + I_{x,1} e^{-i(2\pi/3)} + I_{x,2} e^{i(2\pi/3)}]$. The additional R_x^* term must be considered during the calculation of the coherency matrices. Fortunately, we find the phase part of R_x^* will be automatically erased when we construct the SSM in Eq. (1). On the other hand, the amplitude part of R_x^* remains as a form of $|R_x|^2$, but is compensated by one additional measurement while the sample arm is blocked. As a result, we take a total of $3N + 1$ (10 561) images to calibrate the scattering matrix, which requires about 19 min.

We take the central 512×512 pixels ($M = 262\,144$) of the CCD camera (4242×2830 pixels; 3.1 mm pitch; MD120MU-SY, XIMEA GmbH) for position states $|x\rangle$. Although a greater number of sampling position states provides better results by suppressing the second term in Eq. (2), we could not fully utilize all of the CCD pixels because of limited data storage capacity, and the computing ability of the used computer (3.50 GHz, intel® core™ i5-4690 CPU; 32.0 GB RAM).
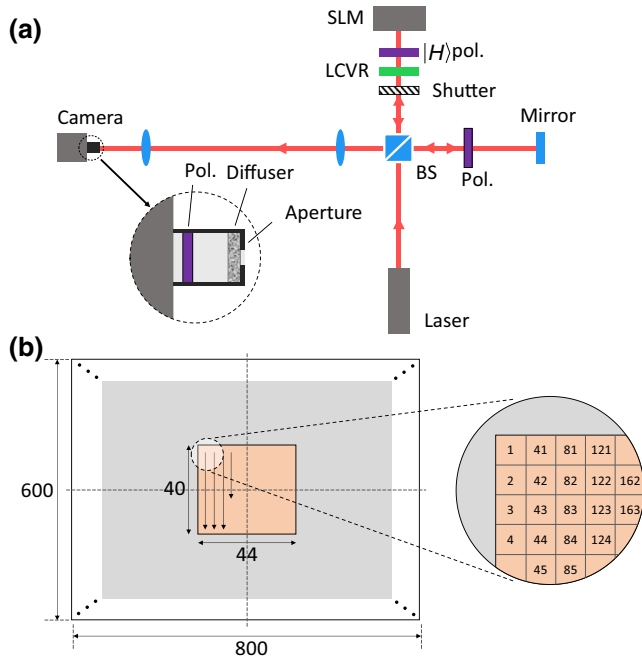
(a)

(b)

FIG. 6. (a) Optical setup for transmission matrix calibration. The definitions of texts are as follows: Laser, unpolarized He-Ne laser (HNL050R, Thorlabs Inc.); BS, 50:50 beam splitter (BS013, Thorlabs Inc.); Shutter, motorized shutter (MFF101/M, Thorlabs Inc.); LCVR, liquid crystal variable retarder (LCC1222-A, Thorlabs Inc.); Pol., polarizer (WP25M-VIS, Thorlabs Inc.); SLM, spatial light modulator (X10468-01, Hamamatsu Photonics K.K.); Camera, CCD camera (MD120MU-SY, XIMEA GmbH). Elements without texts are conventional mirrors and lenses. The 4-f relaying system has a $\times 3$ demagnification factor. The LCVR switches the output polarization state. The shutter is used to block the SLM arm in order to measure the reference speckle pattern. The role of the polarizer on the reference arm is to make a reference state; therefore, the orientation of the polarizer on the reference arm is not important. (b) Calibrated momentum states and their vectorization numbering order. The rectangular (800×600) momentum space of the SLM active area is shown (left). Note that the spacing between the adjacent momentum states is inversely proportional to the clear aperture of the SLM (16×12 mm^2). The direct current (dc, or zero transversal momentum) state is placed on the center of the rectangle. The calibrated momentum states are the central 44×40 rectangle shape, and the ordering is the conventional vectorization order of MATLAB® (right).

The stability of the calibration system [Fig. 6(a)] during the calibration process is confirmed by comparing the speckle patterns before and after the calibration for the same SLM pattern. We observe that the calibrated TM remains stable and valid 24 h after the calibration.

APPENDIX D: POWER SPECTRUM ANALYSIS

In order to find the effective number of sampled optical modes, we calculate the spatial power spectrum of the measured speckle, $S(\mathbf{k})$. Since we measure the 2D intensity
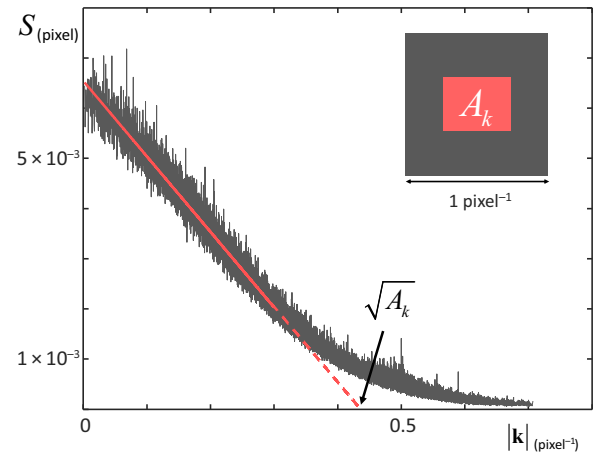

FIG. 7. Power spectrum of speckle. We plot an azimuthally averaged power spectrum $S(|\mathbf{k}|)$, which is linearly decreasing (i.e., triangular distribution) as the $|\mathbf{k}|$ increases. We use the "pixel unit" that indicates the physical pixel size of the used camera as a unit. The inset depicts the effective area A_k of the speckle field span in the reciprocal space. For rectangular windows as in our experiments, the x intercept indicates $\sqrt{A_k} = 0.436$.

speckle $I(\mathbf{x})$, the power spectrums are calculated as the 2D Fourier transform of the intensity speckles

$$S(\mathbf{k}) = \left| \iint I(\mathbf{x}) e^{-i2\pi \mathbf{k}x} d\mathbf{x} \right|^2, \tag{D1}$$

which is the Wiener-Khinchin theorem. A total of $N = 3520$ power spectrums are compounded and then azimuthally averaged to get $S(|\mathbf{k}|)$, which is expected to exhibit a triangular distribution [2].

From the fitted result, we can calculate the effective area A_k that the speckle field spans in the reciprocal space (Fig. 7), which is directly related to the experimental oversampling ratio, $M'/M = A_k^{-1}$. Therefore, we can deduce the $M = 49\,600$ and corresponding M to N ratio $\gamma = 14$.

APPENDIX E: VECTOR FIELD PREPARATION

For the pure states, the initial polarization state is prepared to be $|A\rangle = \frac{1}{\sqrt{2}}|H\rangle - \frac{1}{\sqrt{2}}|V\rangle$, or $\frac{1}{\sqrt{2}}\left(\begin{smallmatrix} 1 \\ -1 \end{smallmatrix}\right)$. Since $|A\rangle$ is the fast axis of the quarter-wave plate, the polarization is maintained before the SLM. The SLM modulates the $|H\rangle$ polarization, and the reflected polarization become $\frac{1}{\sqrt{2}}\left(\begin{smallmatrix} e^{i\varphi_r} \\ 1 \end{smallmatrix}\right)$, where φ_r denotes the phase retardance as the function of the SLM position $|r\rangle$. Note that the sign of $|V\rangle$ is changed due to the reflection geometry of the SLM, $(x, y, z) \rightarrow (x, -y, -z)$. After the quarter-wave plate, the output polarization becomes

$$|s\rangle = e^{i(\varphi_r/2)} \begin{bmatrix} \cos\left(\frac{\varphi_r}{2} + \frac{\pi}{4}\right) \\ \sin\left(\frac{\varphi_r}{2} + \frac{\pi}{4}\right) \end{bmatrix}. \tag{E1}$$

Allocating different phase values over the SLM active plane, the output polarization state exhibits a position dependency called the "vector field."

APPENDIX F: STOKES PARAMETERS MEASUREMENTS

In order to confirm the unpolarized state generated from a He-Ne laser (HNL050R, Thorlabs Inc.), we measure the Stokes parameter by measuring the intensities in six different polarization states. The polarization of the analyzer is changed using a polarizer (LPVISE100-A; Thorlabs Inc.) and a liquid crystal variable retarder (LCVR; LCC1222-A, Thorlabs Inc.). The measured Stokes parameters are (1, 0.006, -0.004, and -0.006), which clearly indicate the unpolarized state.

APPENDIX G: POTENTIAL FACTORS THAT MAY AFFECT THE REQUIRED OVERSAMPLING RATIO

Notice that for optical systems having $g \approx M$, the mean transmittance and the transmission eigenvalue distribution of the optical system may also affect the achievable fidelity.

1. Mean transmittance, $\bar{T}$

The information transmission capacity of the optical system can be quantified by the dimensionless conductance (g) [48]. If we utilize the optical modes that exceed g, we should take the reflective information loss and induced mesoscopic correlation between output speckles addressed in Ref. [48] into account. However, please notice that our experiments have far larger $g = 1.77 \times 10^8$ than the input ($N = 3520$) and output ($M = 49\,600$) optical modes, so the reflective intensity loss does not induce the loss of optical information in our experimental situations

2. The condition number of transmission matrix

Since the SSM can be considered as a nonlinear inversion process, the condition number of the transmission matrix may be an important factor. According to Ref. [48], the eigenvalue ($\tilde{\tau}$) distribution of $\hat{t}^\dagger \hat{t}$, a disordered system having $g \gg M$, follows a Marcenko-Pastur (MP) distribution. The maximum and minimum eigenvalues ($\tilde{\tau}_{\max}$ and $\tilde{\tau}_{\min}$) of the MP distribution are the function of the oversampling ratio (γ), $\tilde{\tau}_{\max} = \langle \tilde{\tau} \rangle (1 + \gamma^{-1/2})^2$ and $\tilde{\tau}_{\min} = \langle \tilde{\tau} \rangle (1 - \gamma^{-1/2})^2$, where $\langle \tilde{\tau} \rangle$ is the mean of the eigenvalues. Then, the condition number of the transmission matrix also becomes the function of γ

$$\text{condition number} = \sqrt{\frac{\tilde{\tau}_{\max}}{\tilde{\tau}_{\min}}} = \frac{\sqrt{\gamma} + 1}{\sqrt{\gamma} - 1} \qquad \text{(G1)}$$

Notice that the condition number decreases as γ increases. Therefore, we can infer that previous numerical results
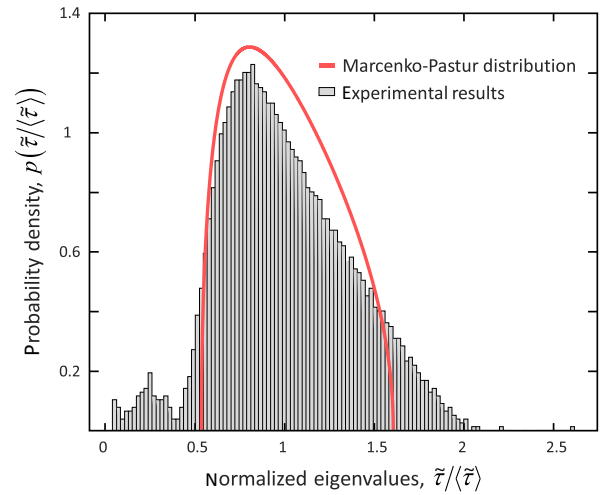

FIG. 8. The histogram of the experimental eigenvalue ($\tilde{\tau}$) distribution of $\hat{t}^\dagger \hat{t}$. The expected MP distribution for $\gamma = 14$ is also shown (red line).

(Fig. 5) already include the effect of the condition number since the effect of γ is already taken into account.

Figure 8 shows the experimental transmission eigenvalue distribution and the MP distribution for $\gamma = 14$. Although the measured condition number (8.00) is far larger than the expected value (1.73), we find the overall trend of eigenvalue distribution follows the MP distribution. We suspect the unexpected tails on the measured eigenvalue distribution are originated from the slight nonzero correlations between the preset planewaves $|p\rangle$ due to the unmodulated portion of the used SLM.

[1] J. C. Dainty, *Laser Speckle and Related Phenomena* (Springer-Verlag, Berlin, Germany, 1975).

[2] J. W. Goodman, *Speckle Phenomena in Optics: Theory and Applications* (Roberts & Company, Englewood, CO, USA, 2007).

[3] N. George, C. R. Christensen, J. S. Bennett, and B. D. Guenther, Speckle noise in displays, J. Opt. Soc. Am. **66**, 1282 (1976).

[4] A. Kozma and C. R. Christensen, Effects of speckle on resolution*, J. Opt. Soc. Am. **66**, 1257 (1976).

[5] J. M. Artigas and A. Felipe, Effect of luminance on photopic visual acuity in the presence of laser speckle, J. Opt. Soc. Am. A **5**, 1767 (1988).

[6] J. A. Leendertz, Interferometric displacement measurement on scattering surfaces utilizing speckle effect, J. Phys. E: Sci. Instrum. **3**, 214 (1970).

[7] D. B. Barker and M. E. Fourney, Measuring fluid velocities with speckle patterns, Opt. Lett. **1**, 135 (1977).

[8] P. V. Farrell and D. L. Hofeldt, Temperature measurement in gases using speckle photography, Appl. Opt. **23**, 1055 (1984).

[9] R. Erf, *Speckle Metrology* (Elsevier Science, New York, NY, USA, 2012).

[10] B. Redding, S. F. Liew, R. Sarma, and H. Cao, Compact spectrometer based on a disordered photonic chip, Nat. Photonics **7,** 746 (2013).

[11] V. Trivedi, S. Mahajan, V. Chhaniwal, Z. Zalevsky, B. Javidi, and A. Anand, Optical temperature sensor using speckle field, Sens. Actuators, A **216,** 312 (2014).

[12] K. Kim, H. Yu, J. Koh, J. H. Shin, W. Lee, and Y. Park, Remote sensing of pressure inside deformable microchannels using light scattering in Scotch tape, Opt. Lett. **41,** 1837 (2016).

[13] S. Popoff, G. Lerosey, M. Fink, A. C. Boccara, and S. Gigan, Image transmission through an opaque material, Nat. Commun. **1,** 81 (2010).

[14] S. M. Popoff, G. Lerosey, R. Carminati, M. Fink, A. C. Boccara, and S. Gigan, Measuring the Transmission Matrix in Optics: An Approach to the Study and Control of Light Propagation in Disordered Media, Phys. Rev. Lett. **104,** 100601 (2010).

[15] Y. Bromberg and H. Cao, Generating Non-Rayleigh Speckles with Tailored Intensity Statistics, Phys. Rev. Lett. **112,** 213904 (2014).

[16] A. J. F. Siegert and M. I. o. T. R. Laboratory, *On the Fluctuations in Signals Returned by Many Independently Moving Scatterers* (Radiation Laboratory, Massachusetts Institute of Technology, Cambridge, MA, USA, 1943).

[17] D. A. Boas and A. K. Dunn, (SPIE, 2010), p. 12.

[18] K. Kim, H. Yu, K. Lee, and Y. Park, Universal sensitivity of speckle intensity correlations to wavefront change in light diffusers, Sci. Rep. **7,** 44435 (2017).

[19] K. Lee and Y. Park, Exploiting the speckle-correlation scattering matrix for a compact reference-free holographic image sensor, Nat. Commun. **7,** 13359 (2016).

[20] Y. Baek, K. Lee, and Y. Park, High-resolution long-working-distance reference-free holographic microscopy exploiting speckle-correlation scattering matrix, arXiv preprint arXiv:1802.10321 (2018).

[21] H. Kwon, E. Arbabi, S. M. Kamali, M. Faraji-Dana, and A. Faraon, Computational complex optical field imaging using a designed metasurface diffuser, Optica **5,** 924 (2018).

[22] T. Čižmár and K. Dholakia, Exploiting multimode waveguides for pure fibre-based imaging, Nat. Commun. **3,** 1027 (2012).

[23] Y. Choi, C. Yoon, M. Kim, T. D. Yang, C. Fang-Yen, R. R. Dasari, K. J. Lee, and W. Choi, Scanner-Free and Wide-Field Endoscopic Imaging by Using a Single Multimode Optical Fiber, Phys. Rev. Lett. **109,** 203901 (2012).

[24] L. Mandel, E. Wolf, and C. U. Press, *Optical Coherence and Quantum Optics* (Cambridge University Press, Cambridge, UK, 1995).

[25] B. E. A. Saleh and M. C. Teich, *Fundamentals of Photonics* (Wiley, Hoboken, NJ, USA, 2013).

[26] E. Jakeman and P. N. Pusey, Non-Gaussian fluctuations in electromagnetic radiation scattered by random phase screen. I. Theory, J. Phys. A: Math. Gen. **8,** 369 (1975).

[27] E. Jakeman and J. G. McWhirter, Non-Gaussian scattering by a random phase screen, Appl. Phys. B **26,** 125 (1981).

[28] P. A. Mello, E. Akkermans, and B. Shapiro, Macroscopic Approach to Correlations in the Electronic Transmission

and Reflection from Disordered Conductors, Phys. Rev. Lett. **61,** 459 (1988).

[29] A. P. Mosk, A. Lagendijk, G. Lerosey, and M. Fink, Controlling waves in space and time for imaging and focusing in complex media, Nat. Photonics **6,** 283 (2012).

[30] G. C. Wick, The evaluation of the collision matrix, Phys. Rev. **80,** 268 (1950).

[31] U. Leonhardt, *Measuring the Quantum State of Light* (Cambridge University Press, Cambridge, UK, 1997).

[32] R. Martínez-Herrero, P. M. Mejías, and G. Piquero, *Characterization of Partially Polarized Light Fields* (Springer, Berlin, Heidelberg, 2009).

[33] F. Gori, M. Santarsiero, and R. Borghi, Vector mode analysis of a Young interferometer, Opt. Lett. **31,** 858 (2006).

[34] K. H. Kagalwala, G. Di Giuseppe, A. F. Abouraddy, and B. E. A. Saleh, Bell's measure in classical optical coherence, Nat. Photonics **7,** 72 (2012).

[35] A. F. Abouraddy, K. H. Kagalwala, and B. E. A. Saleh, Two-point optical coherency matrix tomography, Opt. Lett. **39,** 2411 (2014).

[36] D. Bicout, C. Brosseau, A. S. Martinez, and J. M. Schmitt, Depolarization of multiply scattered waves by spherical diffusers: Iinfluence of the size parameter, Phys. Rev. E **49,** 1767 (1994).

[37] M. Xu and R. R. Alfano, Random Walk of Polarized Light in Turbid Media, Phys. Rev. Lett. **95,** 213901 (2005).

[38] I. M. Vellekoop and A. P. Mosk, Focusing coherent light through opaque strongly scattering media, Opt. Lett. **32,** 2309 (2007).

[39] J.-H. Park, C. Park, H. Yu, Y.-H. Cho, and Y. Park, Active spectral filtering through turbid media, Opt. Lett. **37,** 3261 (2012).

[40] J.-H. Park, C. Park, H. Yu, Y.-H. Cho, and Y. Park, Dynamic active wave plate using random nanoparticles, Opt. Express **20,** 17010 (2012).

[41] O. N. Dorokhov, On the coexistence of localized and extended electronic states in the metallic phase, Solid State Commun. **51,** 381 (1984).

[42] Y. Imry, Active transmission channels and universal conductance fluctuations, Europhys. Lett. **1,** 249 (1986).

[43] Y. V. Nazarov, Limits of Universality in Disordered Conductors, Phys. Rev. Lett. **73,** 134 (1994).

[44] M. C. W. van Rossum and T. M. Nieuwenhuizen, Multiple scattering of classical waves: Microscopy, mesoscopy, and diffusion, Rev. Mod. Phys. **71,** 313 (1999).

[45] S. Rotter and S. Gigan, Light fields in complex media: Mesoscopic scattering meets wave control, Rev. Mod. Phys. **89,** 015005 (2017).

[46] R. Horisaki, R. Egami, and J. Tanida, Single-shot phase imaging with randomized light (SPIRaL), Opt. Express **24,** 3765 (2016).

[47] J. R. DeVore, Refractive indices of rutile and sphalerite, J. Opt. Soc. Am. **41,** 416 (1951).

[48] C. W. Hsu, S. F. Liew, A. Goetschy, H. Cao, and A. Douglas Stone, Correlation-enhanced control of wave focusing in disordered media, Nat. Phys. **13,** 497 (2017).

[49] J. Yoon, K. Lee, J. Park, and Y. Park, Measuring optical transmission matrices by wavefront shaping, Opt. Express **23,** 10158 (2015).

[50] Q. Zhan, Cylindrical vector beams: From mathematical concepts to applications, Adv. Opt. Photon. **1**, 1 (2009).

[51] K. Lee and Y. Park, MATLAB code, figshare (2019) [retrieved 13 March, 2019], 10.6084/m9.figshare.7835516.v2.

[52] R. Jozsa, Fidelity for mixed quantum states, J. Mod. Opt. **41**, 2315 (1994).

[53] J. Ellis and A. Dogariu, Optical Polarimetry of Random Fields, Phys. Rev. Lett. **95**, 203905 (2005).

[54] R. F. Wagner, S. W. Smith, J. M. Sandrik, and H. Lopez, Statistics of speckle in ultrasound B-scans, IEEE Trans. Sonics Ultrason. **30**, 156 (1983).

[55] J. Wang and A. Z. Genack, Transport through modes in random media, Nature **471**, 345 (2011).

[56] M. Sutton, S. G. J. Mochrie, T. Greytak, S. E. Nagler, L. E. Berman, G. A. Held, and G. B. Stephenson, Observation of speckle by diffraction with coherent X-rays, Nature **352**, 608 (1991).

[57] M. Jang, Y. Horie, A. Shibukawa, J. Brake, Y. Liu, S. M. Kamali, A. Arbabi, H. Ruan, A. Faraon, and C. Yang, Wavefront shaping with disorder-engineered metasurfaces, Nat. Photonics **12**, 84 (2018).

[58] J. Park, K. Lee, and Y. Park, Ultrathin wide-angle large-area digital 3D holographic display using a non-periodic photon sieve, Nat. Commun. **10**, 1304 (2019).